ACS OMEGA

http://pubs.acs.org/journal/acsodf

Article

# Machine Learning Band Gaps of Doped-$TiO_2$ Photocatalysts from Structural and Morphological Parameters

Yun Zhang* and Xiaojie Xu*

Cite This: *ACS Omega* 2020, 5, 15344−15352

Read Online

ACCESS | Metrics & More | Article Recommendations

**ABSTRACT:** Titanium dioxide ($TiO_2$) photocatalysts in the form of thin films are of great interest due to their tunable optical band gaps, $E_g$'s, which are promising candidates for applications of visible-light photocatalytic activities. Previous studies have shown that processing conditions, dopant types and concentrations, and different combinations of the two have great impacts on structural, microscopic, and optical properties of $TiO_2$ thin films. The lattice parameters and surface area are strongly correlated with $E_g$ values, which are conventionally simulated and studied through first-principle models, but these models require significant computational resources, particularly in complex situations involving codoping and various surface areas. In this study, we develop the Gaussian process regression model for predictions of anatase $TiO_2$ photocatalysts' energy band gaps based on the lattice parameters and surface area. We explore 60 doped-$TiO_2$ anatase photocatalysts with $E_g$'s between 2.280 and 3.250 eV. Our model demonstrates a high correlation coefficient of 99.99% between predicted $E_g$'s and their experimental values and high prediction accuracy as reflected through the prediction root-mean-square error and mean absolute error being 0.0012 and 0.0010% of the average experimental $E_g$, respectively. This modeling method is simple and straightforward and does not require a lot of parameters, which are advantages for applications and computations.

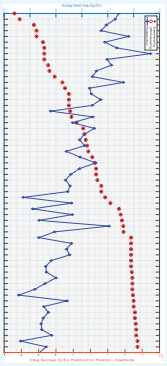

## 1. INTRODUCTION

Titanium dioxide, $TiO_2$, shows great promises in several environmental applications due to its distinct properties over other materials, such as the nontoxicity, low cost, ease of preparation, water insolubility, superior acid resistance, and superhydrophilicity.[1] Examples of application areas include the air purification, water treatment, renewable energy processes, solar cells, and conversion of $CO_2$ to hydrocarbons.[2−6] Among $TiO_2$ polymorphs, anatase $TiO_2$ is preferred over brookite and rutile because it has a higher surface energy of its {001} facets and better photocatalytic activities and is more stable than the other two forms. However, anatase $TiO_2$ has a relatively wide band gap (~3.20 eV), which only allows the material to absorb UV light. As UV light only accounts for merely 5% of solar photons, the large band gap of $TiO_2$ limits the quantum yield in light-to-energy conversion.[7−10]

One effective way to modify the band gap of anatase $TiO_2$ is chemical doping with foreign elements. Different elements, metals and nonmetals, affect the band gap in different ways. Metal ions, such as Zr, Cr, and W, are reported to inhibit the anatase-to-rutile phase transformation.[11,12] Transition metals, such as Cu, and rare-earth metals, such as La, lead to the lattice deformation and the formation of oxygen vacancies, resulting in an impurity state in the $TiO_2$ band gap, which improves the absorption of visible light by narrowing the band gap.[13,14] Nonmetal doping, such as the nitrogen incorporation into the $TiO_2$ lattice or on its surface, has been reported to benefit the improvement of photoefficiency under UV/visible light.[1] Both single doping and codoping methods have been applied to the $TiO_2$ photocatalyst fabrication by incorporating various elements into the crystal structure.[10,13−24] The addition of foreign elements results in lattice distortions and changes in the $E_g$ due to electronegativities, ionic radius differences, and introductions of impurity states.[25] In addition to chemical doping, various preparation methods of $TiO_2$ photocatalysts can influence the band gap narrowing differently. Typical fabrication methods include the coprecipitation, sol−gel process, spray pyrolysis, hydrothermal process, low-temperature solvothermal method, and plasma treatment.[13,18,20,21] Processing parameters, including but not limited to the precursor materials, substrate temperature, deposition rate, and annealing temperature, affect the crystal structure and microstructure significantly. As a result, lattice parameters and the surface area are changed upon different combinations of synthesis steps.[1,25−29] Previous research has demonstrated that the photocatalytic activity of $TiO_2$ strongly depends on its phase structure, crystallinity, and morphology.[30,31] Among various phases of $TiO_2$, anatase is reported to have a better photocatalytic activity than the other two polymorphs.[32] A good crystallinity is required to achieve the formation of an optimal amount of electron traps, which affects

**Received:** March 30, 2020
**Accepted:** June 8, 2020
**Published:** June 16, 2020

**Table 1. Experimental Data and Predictions**[a]

| sample | $a$ (Å) | $c$ (Å) | surface area ($m^2/g$) | $E_g$ (eV) | prediction | reference |
|---|---|---|---|---|---|---|
| pure $TiO_2$ | 3.7650 | 9.4860 | 43.00 | 3.122 | 3.12198 | 21 |
| 1.0% Cu−3.5% In−$TiO_2$ | 3.7760 | 9.4620 | 85.00 | 3.087 | 3.08695 | 21 |
| 5 mol % Cu-doped $TiO_2$ (700°C) | 3.7700 | 6.0190 | 110.70 | 2.430 | 2.43004 | 15 |
| 5 mol % Cu-doped $TiO_2$ (600°C) | 3.7960 | 9.4310 | 150.90 | 2.510 | 2.51004 | 15 |
| 5 mol % Cu, 15 mol % Zr co-doped $TiO_2$ (700 °C) | 3.8340 | 11.4420 | 127.20 | 2.280 | 2.28005 | 15 |
| 5 mol % Cu, 15 mol % Zr co-doped $TiO_2$ (600 °C) | 3.8080 | 10.0000 | 156.60 | 2.320 | 2.32005 | 15 |
| undoped-$TiO_2$ | 3.7900 | 9.6300 | 146.07 | 2.950 | 2.94999 | 20 |
| S-doped $TiO_2$ ($K_2S_2O_8$/Ti = 0.25) | 3.7800 | 9.5900 | 183.45 | 2.850 | 2.84999 | 20 |
| S-doped $TiO_2$ ($K_2S_2O_8$/Ti = 0.5) | 3.7900 | 9.5800 | 216.22 | 2.830 | 2.83001 | 20 |
| pure $TiO_2$ | 3.7740 | 9.4480 | 44.80 | 3.230 | 3.22994 | 10 |
| $S_{0.05}/TiO_2$ | 3.7750 | 9.5480 | 48.60 | 2.950 | 2.95000 | 10 |
| $S_{0.05}V_{0.001}/TiO_2$ | 3.7770 | 9.4610 | 64.40 | 2.810 | 2.81002 | 10 |
| $S_{0.05}Fe_{0.001}/TiO_2$ | 3.7820 | 9.6670 | 66.60 | 2.880 | 2.88001 | 10 |
| $S_{0.05}Zn_{0.001}/TiO_2$ | 3.7930 | 9.4140 | 61.80 | 3.230 | 3.22997 | 10 |
| undoped-$TiO_2$ | 3.7848 | 9.4826 | 216.00 | 3.110 | 3.10996 | 19 |
| V-doped $TiO_2$ | 3.7882 | 9.4949 | 203.00 | 2.910 | 2.91000 | 19 |
| N-doped $TiO_2$ | 3.7917 | 9.4868 | 181.00 | 2.920 | 2.91999 | 19 |
| V,N co-doped $TiO_2$ | 3.7996 | 9.4976 | 172.00 | 2.760 | 2.76000 | 19 |
| pure $TiO_2$ | 3.7860 | 9.5260 | 80.37 | 3.180 | 3.17999 | 13 |
| N−$TiO_2$ | 3.7850 | 9.4710 | 96.49 | 2.900 | 2.90003 | 13 |
| La−$TiO_2$ | 3.7800 | 9.5180 | 89.42 | 3.020 | 3.02000 | 13 |
| N/La−$TiO_2$ | 3.7860 | 9.4780 | 116.25 | 2.840 | 2.84001 | 13 |
| undoped-$TiO_2$ | 3.7760 | 9.4860 | 51.30 | 2.910 | 2.91001 | 18 |
| Ce-doped $TiO_2$, "$C_{0.03}T_1$" | 3.7740 | 9.4540 | 63.52 | 2.720 | 2.72002 | 18 |
| Ce-doped $TiO_2$, "$C_{0.01}T_1$" | 3.7720 | 9.4420 | 67.43 | 2.670 | 2.67002 | 18 |
| Ce-doped $TiO_2$, "$C_{0.05}T_1$" | 3.7710 | 9.4500 | 60.14 | 2.700 | 2.70002 | 18 |
| Ce,Si co-doped $TiO_2$, "$C_{0.01}T_1S_{0.05}$" | 3.7700 | 9.4570 | 102.41 | 2.650 | 2.65006 | 18 |
| Ce,Si co-doped $TiO_2$, "$C_{0.01}T_1S_{0.5}$" | 3.7600 | 9.4620 | 164.48 | 2.510 | 2.51005 | 18 |
| Ce,Si co-doped $TiO_2$, "$C_{0.01}T_1S_1$" | 3.7600 | 9.4810 | 168.54 | 2.710 | 2.70997 | 18 |
| Ce-doped $TiO_2$, "$C_{0.005}T_1$" | 3.7580 | 9.4420 | 53.57 | 2.820 | 2.82001 | 18 |
| undoped-$TiO_2$ (475 °C) | 3.8220 | 10.6100 | 71.40 | 3.210 | 3.20997 | 14 |
| Ce(2%)Co(4%)−$TiO_2$ (600 °C) | 3.8060 | 11.1800 | 43.60 | 3.200 | 3.19997 | 14 |
| Ce(2%)Co(4%)−$TiO_2$ (700 °C) | 3.8130 | 10.0000 | 39.80 | 3.180 | 3.17997 | 14 |
| undoped-$TiO_2$ | 3.7760 | 9.3410 | 85.93 | 3.220 | 3.21996 | 24 |
| 1% Nb-doped $TiO_2$ | 3.7860 | 9.3470 | 150.61 | 3.250 | 3.24996 | 24 |
| pure $TiO_2$ | 3.7760 | 9.4860 | 67.70 | 2.980 | 2.97994 | 17 |
| Ag-doped $TiO_2$(400 °C) | 3.7822 | 9.5023 | 106.37 | 2.450 | 2.45006 | 17 |
| Ag-doped $TiO_2$ (500 °C) | 3.7770 | 9.5010 | 78.40 | 2.510 | 2.51009 | 17 |
| Ag-doped $TiO_2$ (600 °C) | 3.7760 | 9.4860 | 29.33 | 2.540 | 2.54004 | 17 |
| Ag-doped $TiO_2$ (700 °C) | 3.7822 | 9.5023 | 1.93 | 2.590 | 2.59002 | 17 |
| undoped-$TiO_2$ | 3.7945 | 9.5079 | 37.90 | 3.180 | 3.17997 | 16 |
| 1 wt % Mn-doped $TiO_2$ | 3.7945 | 9.4860 | 52.59 | 3.100 | 3.10000 | 16 |
| 5 wt % Mn-doped $TiO_2$ | 3.7956 | 9.4993 | 80.77 | 2.700 | 2.70002 | 16 |
| 10 wt % Mn-doped $TiO_2$ | 3.7922 | 9.4546 | 95.19 | 2.700 | 2.70003 | 16 |
| 20 wt % Mn-doped $TiO_2$ (TMA400) | 3.7762 | 9.4681 | 212.71 | 2.450 | 2.45003 | 16 |
| 20 wt % Mn-doped $TiO_2$ (TMB400) | 3.7808 | 9.4720 | 203.00 | 2.500 | 2.50004 | 16 |
| 20 wt % Mn-doped $TiO_2$ (TMN400) | 3.8014 | 9.4105 | 205.36 | 2.550 | 2.55003 | 16 |
| pure $TiO_2$ | 3.7835 | 9.4907 | 86.11 | 3.180 | 3.18000 | 22 |
| 0.05 wt % W-doped $TiO_2$ | 3.7858 | 9.4862 | 88.14 | 3.190 | 3.18997 | 22 |
| 0.1 wt % W-doped $TiO_2$ | 3.7858 | 9.4817 | 86.08 | 3.120 | 3.12004 | 22 |
| 0.5 wt % W-doped $TiO_2$ | 3.7813 | 9.4773 | 91.71 | 3.180 | 3.17996 | 22 |
| 1 wt % W-doped $TiO_2$ | 3.7835 | 9.4817 | 88.18 | 3.190 | 3.18998 | 22 |
| pure $TiO_2$ | 3.7850 | 9.5021 | 59.00 | 3.220 | 3.21998 | 23 |
| 0.1 mol % Sn-doped $TiO_2$ | 3.7864 | 9.4958 | 66.00 | 3.200 | 3.19999 | 23 |
| 0.5 mol % Sn-doped $TiO_2$ | 3.7863 | 9.4927 | 75.00 | 3.180 | 3.18000 | 23 |
| 1 mol % Sn-doped $TiO_2$ | 3.7866 | 9.4915 | 87.00 | 3.210 | 3.20997 | 23 |
| 3 mol % Sn-doped $TiO_2$ | 3.7878 | 9.4884 | 106.00 | 3.190 | 3.18996 | 23 |
| 2.0% In−$TiO_2$ | 3.7630 | 9.4740 | 62.00 | 3.186 | 3.18597 | 21 |
| 3.5% In−$TiO_2$ | 3.7680 | 9.4620 | 98.00 | 3.195 | 3.19494 | 21 |
| 5.0% In−$TiO_2$ | 3.7920 | 9.4360 | 123.00 | 3.217 | 3.21696 | 21 |
| minimum | 3.7580 | 6.0190 | 1.93 | 2.280 | 2.28005 | |



https://dx.doi.org/10.1021/acsomega.0c01438
ACS Omega 2020, 5, 15344−15352

**Table 1. continued**

| sample | $a$ (Å) | $c$ (Å) | surface area ($m^2/g$) | $E_g$ (eV) | prediction | reference |
|---|---|---|---|---|---|---|
| mean | 3.7843 | 9.5220 | 101.17 | 2.910 | 2.90962 | |
| median | 3.7842 | 9.4860 | 86.56 | 2.935 | 2.93499 | |
| maximum | 3.8340 | 11.4420 | 216.22 | 3.250 | 3.24996 | |
| standard deviation | 0.0141 | 0.5906 | 53.67 | 0.285 | 0.28542 | |
| correlation coefficient with $E_g$ | 0.76% | 10.59% | −34.18% | | 99.99% | |

[a]"$E_g$ (eV)" and "prediction" represent the experimental and GPR predicted band gaps, respectively, which are visualized in Figure 3.

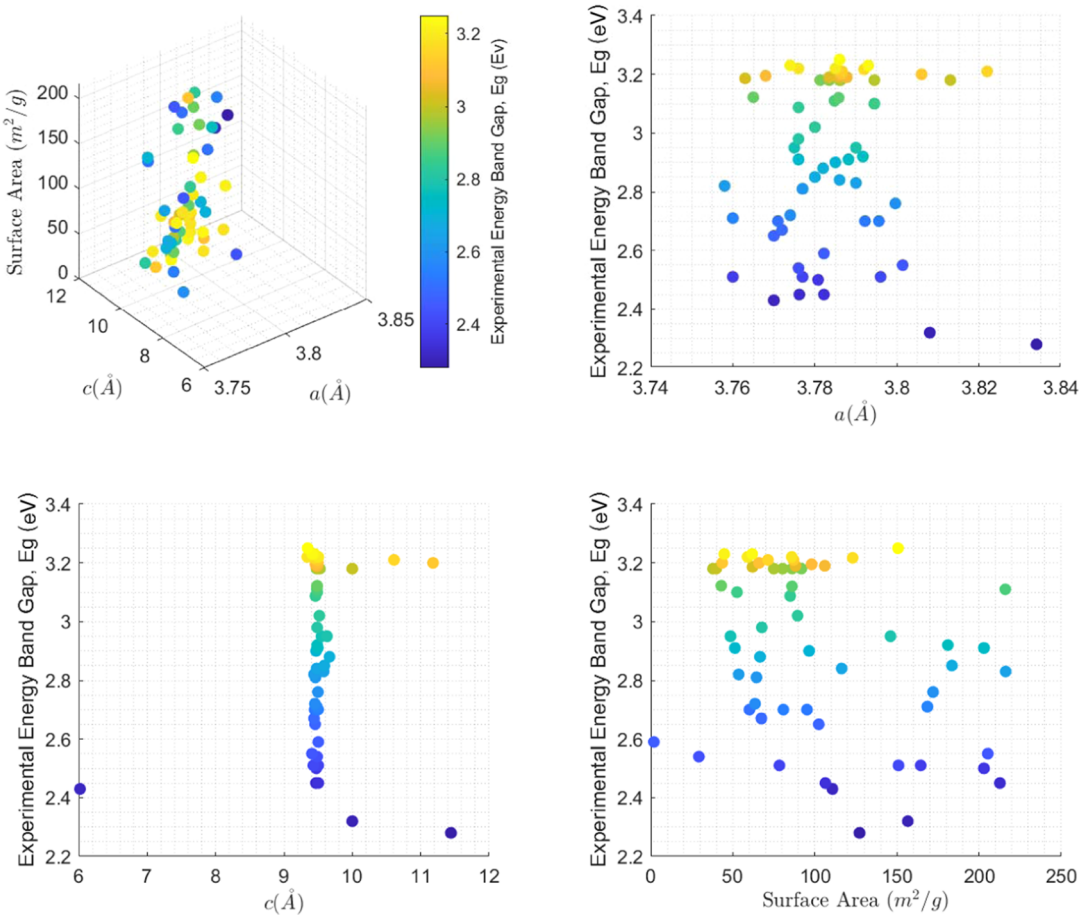


**Figure 1.** Data visualization.

the photocatalytic efficiency. Lattice deformation caused by nonequilibrium crystal growth and chemical doping affects the electronic structure by modifying orbital hybridization and introducing additionally available electrons for conduction.[33,34] Both the crystallinity and lattice deformation can be characterized by lattice parameters. Furthermore, other crystal defects, such as residual strain, impurities, dislocation densities, and defect energy, have significant influences on band gap structures and are correlated with surface morphology, which can be characterized by the surface area.[35,36] High surface areas also promote quantum confinement effects in the semiconductor space charge and surface reaction, which greatly increase the photocatalytic efficiency.[37] For example, N-doped $TiO_2$ obtained by the reduction-nitridation method via the nonthermal plasma treatment is more favorable than the simple nitridation treatment, as the former promotes Ns doping and narrows the band gap more efficiently.[38] Further, the recombination of photogenerated electron-hole pairs limits the photocatalytic activity. Some research has been carried out to reduce the recombination rate of the photoelectron−hole pairs and increase the interfacial charge-transfer efficiency. The surface microstructure, mainly characterized by the surface area, shows additional influences on photocatalyst quality and optical performance. The surface area is correlated with the residual strain, dislocation density, crystallinity, defect energy, impurities, and other structural defects and is shown to contribute to the band gap of $TiO_2$ structures.[35,36] Hence, with various synthesis methods and dopant selection, combination possibilities of $TiO_2$ with the tunable $E_g$ are enormous. It is, therefore, of great importance to investigate correlations among the tunability of the $E_g$, lattice parameters, and the surface area. Qualitative analysis on the effect of dopant types and levels on the $E_g$ of $TiO_2$ photocatalysts has been conducted through experiments.[10,13−24] Quantitative analysis through thermodynamics models and first-principle models has been utilized to aid the understanding of the optical performance of these materials and facilitate the tuning of doped-$TiO_2$ $E_g$.[39,40] However, these models require a significant amount of data inputs, such as


https://dx.doi.org/10.1021/acsomega.0c01438
ACS Omega 2020, 5, 15344−15352

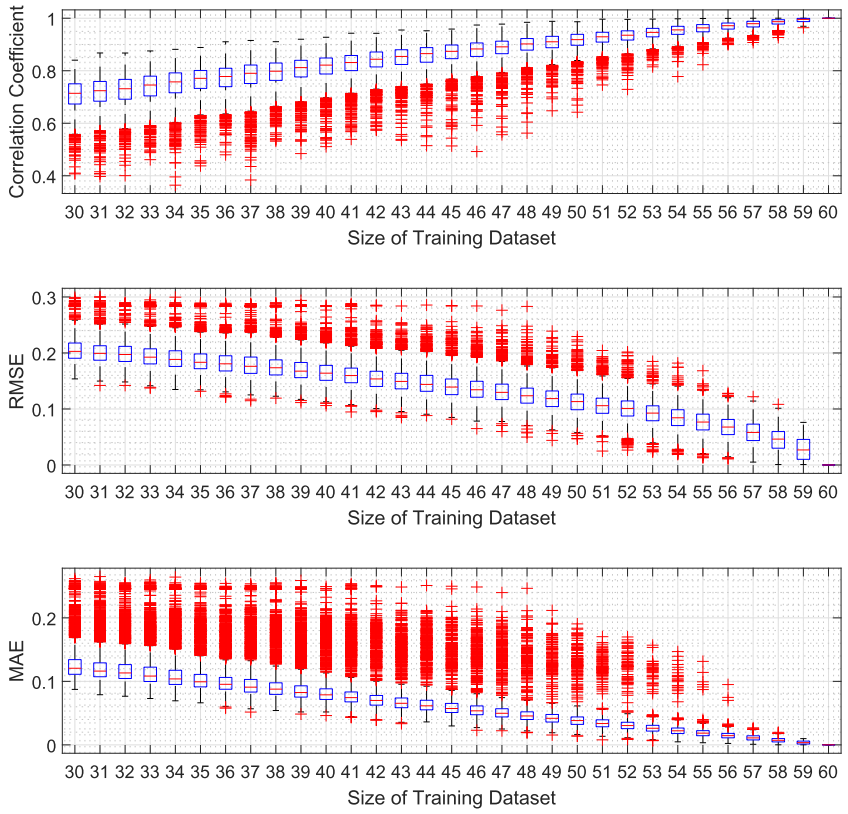


**Figure 2.** Model performance and training data sizes. When the training data set size is between 30 and 57, 2000 random subsamples are drawn without replacements from the whole sample for model training. When the training data set size is 58, 59, or 60, ${}_{60}C_{58}$, ${}_{60}C_{59}$, or ${}_{60}C_{60}$ subsamples are drawn without replacements from the whole sample based on exhaustive sampling for model training. Each trained model based on a certain subsample is used to score the whole sample and obtain the associated model performance. The GPR here uses the exponential kernel and constant basis function, with standardized predictors. Given a model performance measure, box plots show the median, 25th percentile, and 75th percentile. The whiskers extend to the most extreme values (i.e., ±2.7 standard deviation coverage) not considered as outliers, and the outliers are plotted using the "+" symbol.

variables for equations of state and orbital configurations, which can only be obtained by extensive measurements. The requirement of computational power also increases significantly when it comes to the codoping situation.

In this work, the Gaussian process regression (GPR) model is developed to elucidate the statistical relationship among the lattice parameters, $a$ (Å) and $c$ (Å), surface area, and energy band gap for doped-$TiO_2$ anatase photocatalysts. Among the three descriptors, lattice parameters are structural parameters as direct representatives of the phase structure and crystallinity, and the surface area is the morphological parameter. Empirical studies show that crystal defects introduced by doping, such as foreign ions at substitutional or interstitial lattice positions, can shift the band gap toward the visible-light region. Depending on ionic radii, electronegativities, and valence, however, specific types and extents of crystal defects are difficult to estimate. Experimentally, crystal defects require significant amounts of analytical work to characterize, which eventually may be used as inputs into further theoretical work. First-principle simulations calculate the probability of each type of defects and their effects on the band gap tuning based on known atomic interactions, but these methods are known to be susceptible of underestimations of $E_g$ values, particularly when the $TiO_2$ lattices are doped with transition metals.[41,42] Besides, effects of the morphological parameter, the surface area, on $E_g$ values are difficult to incorporate into first-principle simulations. Although a high surface area is generally preferred, it is hard to quantify the required surface area while also considering lattice deformation in a practical application. Our GPR model, however, avoids depending on quantum mechanics theories for calculations, which may be susceptible to over- or underestimations due to unknown atomic interactions. In this method, the known experimental lattice parameters are used as macroscopic descriptors to find the relationship with experimentally measured $E_g$ values. The model generalizes well in the presence of a few descriptive features, where intelligent algorithms are able to learn and recognize the patterns. This modeling approach demonstrates a high degree of accuracy and stability, contributing to efficient and low-cost estimations of the energy band gap of anatase $TiO_2$ and understandings of which are based on the lattice parameters and surface area. As one of the computational intelligence techniques, the GPR model has already been utilized in other materials systems to predict significant physical parameters in different fields of applications.[43−45] This model can serve as a guideline for searching for anatase $TiO_2$ with tunable $E_g$ when a specific range of band gaps is required for a practical application. It can also be used as part of machine learning to aid understandings of the effects of crystal structures and morphology on the optical performance of $TiO_2$ photocatalysts.

The remaining of this work is organized as follows. Section 2 describes the data. Section 3 presents and discusses results, and Section 4 concludes. Section 5 contains details of the GPR model.



https://dx.doi.org/10.1021/acsomega.0c01438
ACS Omega 2020, 5, 15344−15352

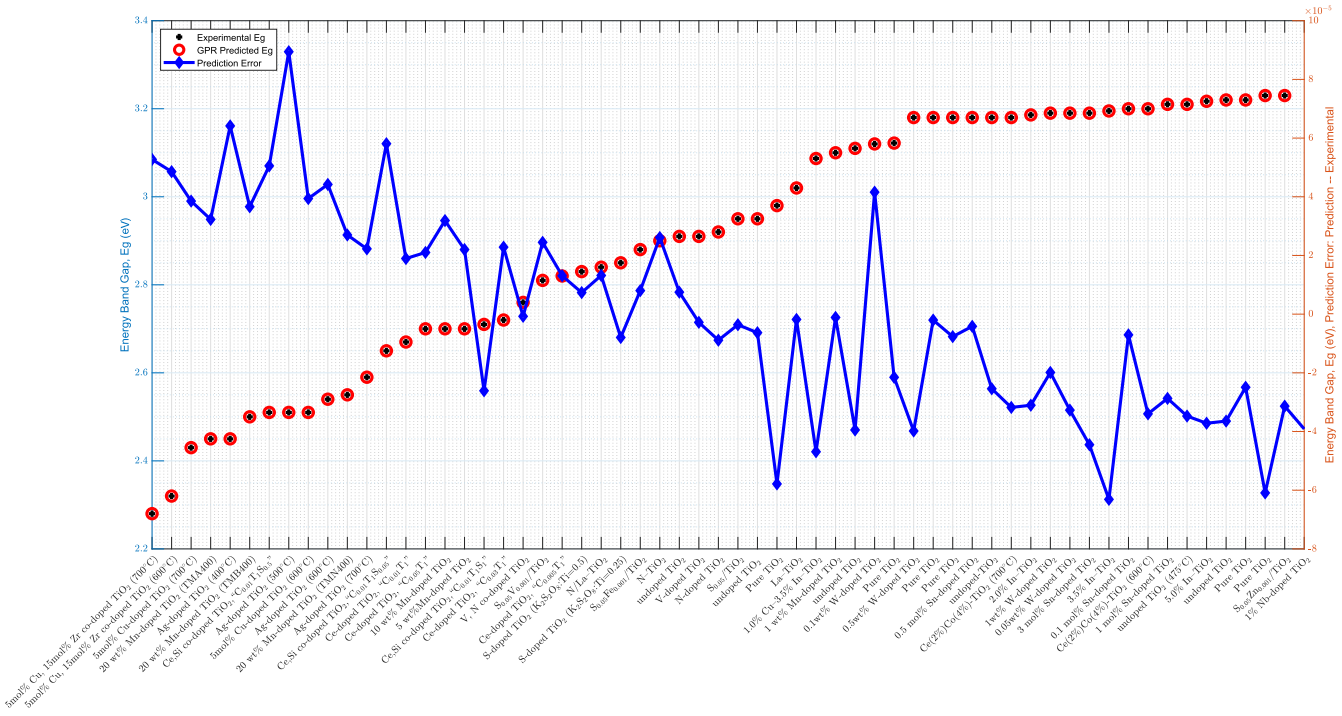


**Figure 3.** Experimental vs predicted $E_g$. The final GPR model is built using the whole sample with the exponential kernel, constant basis function, and standardized predictors. It has a log-likelihood of −3.5784, $\hat{\beta}$ of 2.8382, $\hat{\sigma}$ of 0.0029, $\hat{\sigma}_l$ of 0.2896, and $\hat{\sigma}_f$ of 0.2939. Detailed numerical predictions are listed in Table 1 (column 6).

## 2. DESCRIPTION OF DATA SET

The experimental data used, shown in Table 1 (columns 1−5), are obtained from the literature.[10,13−24] The data set covers a wide range of anatase $TiO_2$ that are prepared through different synthesis methods and doped with various elements. A total of 60 $TiO_2$ photocatalysts with the energy band gap, $E_g$, ranging from 2.280 to 3.250 eV are explored. The lattice parameters, $a$ (Å) and $c$ (Å), and measured surface area are used as descriptors. $E_g$ values are calculated using the Tauc relationship[13,22] after acquiring the transmittance data by the UV−vis spectrometer in each reference in Table 1. Data visualization in Figure 1 reveals nonlinear relationships, which are modeled through the GPR.

## 3. RESULTS AND DISCUSSION

**3.1. Computational Methodology.** MATLAB is utilized for computations and simulations in this work. The relationship between model performance and training data sizes is investigated in Figure 2, which shows the benefit of training the GPR using all observations. The stability of the GPR approach is confirmed by bootstrap analysis in Section 3.3.

**3.2. Prediction Accuracy.** Metal ions, such as $Sn^{4+}$, $Zr^{4+}$, and $Cu^{2+}$, are incorporated into the anatase structure by the substitution of $Ti^{4+}$ due to similar ionic radii, while $Ag^{+}$ is favorably stabilized at an interstitial site. Nonmetal ions, such as N and S, are incorporated into the lattice and coexisted at both substitutional and interstitial sites. Changes in lattice parameters depend on ionic radii, electronegativities, valence, and incorporation mechanisms. On one hand, these crystal defects allow additional electronic levels to be created in the band structure, which effectively narrow the band gap, shift the absorption edge to the visible region, and enhance photocatalytic efficiency. On the other hand, excess additions of some dopants, such as N, may lead to the formation of the oxygen vacancy and $Ti^{3+}$ due to charge imbalance, which increase the charge carrier recombination and hinder conversion efficiency. Hence, codoping is carried out to maintain the charge balance through charge compensation, add new electronic levels, suppress the recombination of charge carriers, and further increase photocatalytic efficiency. Besides, dopants also have an influence on the stability of the anatase phase and surface area. For example, dopants, such as Zr, Ag, W, Ce, and Nb, are found to inhibit the anatase-to-rutile phase transformation, while Mn, Cu, and Co are found to promote it. During the $TiO_2$ synthesis, the high-temperature calcination is usually carried out to achieve high crystallinity, which, however, might lead to extensive grain coarsening and surface area reductions. Additions of dopants that inhibit the phase transformation to structure help stabilize the anatase phase at elevated processing temperature, hinder grain growth, decrease crystallite sizes, and thus increase the surface area. A high surface area indicates increased structural defects on the surface, such as unsaturated surface cations and surface hydroxyl groups, which favor the simultaneous absorption of organic molecules and enhance the photocatalytic efficiency. It should be pointed out that effects of modified lattices and surface areas on band gap tuning and photocatalytic properties are synergistic. There is no linear or monotonic relationship between lattice parameters, surface areas, and band gaps. In this work, the developed model is able to learn and capture the synergistic effects of the structure and morphology on $E_g$ values.

The final GPR model is detailed in Figure 3, which shows a good alignment between predicted and experimental data. The correlation coefficient (CC), root-mean-square error (RMSE), and mean absolute error (MAE) are 99.99%, 0.00003442 (0.0012% of the average experimental $E_g$), and 0.00002872 (0.0010% of the average experimental $E_g$), respectively, representing good prediction performance.


https://dx.doi.org/10.1021/acsomega.0c01438
ACS Omega 2020, 5, 15344−15352

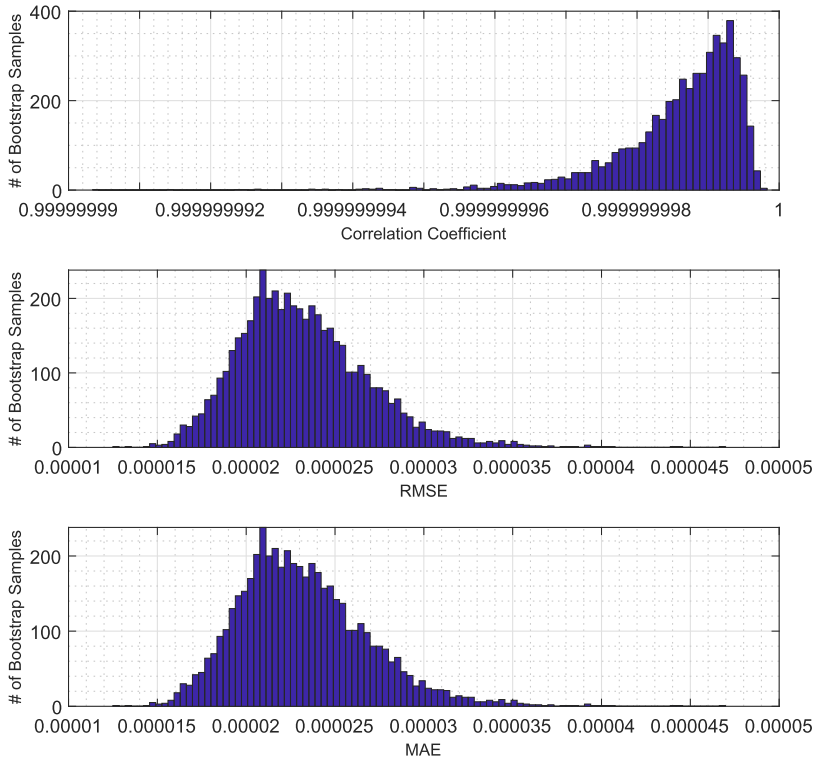


**Figure 4.** Bootstrap analysis of GPR prediction stability. Five thousand bootstrap samples are drawn with replacements from the whole sample. Each bootstrap sample is used to train the GPR based on the exponential kernel, constant basis function, and standardized predictors and obtain the associate model performance. The histograms show distributions of CC, RMSE, and MAE over the 5000 bootstrap samples, whose averages are 99.99%, 0.00002320, and 0.00001782, respectively.

**Table 2. GPR Prediction Sensitivities to Choices of Kernels and Basis Functions**[a]

| kernel | basis function | CC (%) | RMSE | RMSE/sample mean (%) | MAE | MAE/sample mean (%) |
|---|---|---|---|---|---|---|
| exponential | constant | 99.99 | 0.00003442 | 0.0012 | 0.00002872 | 0.0010 |
| exponential | empty | 82.38 | 0.17850737 | 6.1343 | 0.15125528 | 5.1978 |
| exponential | linear | 99.99 | 0.00003472 | 0.0012 | 0.00002926 | 0.0010 |
| exponential | pure quadratic | 99.99 | 0.00003554 | 0.0012 | 0.00002975 | 0.0010 |
| squared exponential | constant | 71.48 | 0.21057940 | 7.2364 | 0.18170821 | 6.2443 |
| matern 5/2 | constant | 99.99 | 0.00007681 | 0.0026 | 0.00005651 | 0.0019 |
| rational quadratic | constant | 99.98 | 0.00630021 | 0.2165 | 0.00459014 | 0.1577 |

[a]The final GPR model is based on the exponential kernel and constant basis function, with standardized predictors.

**3.3. Prediction Stability.** Given the relatively small sample size (see Table 1) used, the prediction stability of the GPR is assessed through bootstrap analysis in Figure 4, which shows that the modeling approach maintains high CCs, low RMSEs, and low MAEs over the bootstrap samples. This result suggests that the GPR might be generalized for $E_g$ modeling of anatase $TiO_2$ based on larger samples.

**3.4. Prediction Sensitivity.** Table 2 shows that the exponential kernel is generally the optimal choice among kernels considered. With the exponential kernel, prediction results are not sensitive to choices of basis functions except for the case of the empty basis function. Given the exponential kernel, the constant basis function is selected as the final specification for its simplicity, which usually is a benefit to model generalization, and its slight better performance as compared to more complicated basis functions, such as linear and pure quadratic.

## 4. CONCLUSIONS

In this study, we develop the Gaussian process regression (GPR) model for predictions of anatase $TiO_2$ photocatalysts' energy band gaps, $E_g$'s, based on the lattice parameters and surface area. Our model demonstrates a high correlation coefficient of 99.99% between predicted $E_g$'s and their experimental values. In addition, the model shows high prediction accuracy as reflected through the prediction root-mean-square error and mean absolute error being 0.0012 and 0.0010% of the average experimental $E_g$, respectively. Finally, model performance is illustrated to be stable. These results suggest that the GPR should be useful to model and understand relationships between structural and morphological parameters and $E_g$'s. This modeling method is simple and straightforward and does not require a lot of parameters, which are advantages for applications and computations. The model can be applied to a wide range of undoped and doped-$TiO_2$ made by various synthesis methods and utilized to facilitate design and understandings of multi-doped $TiO_2$ photocatalysts with tunable $E_g$'s.


https://dx.doi.org/10.1021/acsomega.0c01438
ACS Omega 2020, 5, 15344−15352

## 5. PROPOSED METHODOLOGY

### 5.1. Brief Description of Gaussian Process Regression.

GPRs are nonparametric kernel-based probabilistic models. Consider a training data set, $\{(x_i, y_i); i = 1, 2, ..., n\}$ where $x_i \in \mathbb{R}^d$ and $y_i \in \mathbb{R}$, from an unknown distribution. A trained GPR predicts values of the response variable $y^{new}$ given an input matrix $x^{new}$.

Recall a linear regression model, $y = x^T\beta + \varepsilon$, where $\varepsilon \sim N(0, \sigma^2)$. A GPR aims at explaining $y$ by introducing latent variables, $l(x_i)$ where $i = 1, 2, ..., n$, from a Gaussian process such that the joint distribution of $l(x_i)s$ is Gaussian and explicit basis functions, $b$. The covariance function of $l(x_i)$ captures the smoothness of $y$, and basis functions project $x$ into a feature space of dimension $p$.

A GP is defined by the mean and covariance. Let $m(x) = E(l(x))$ be the mean function and $k(x, x') = \mathrm{Cov}[l(x), l(x')]$ the covariance function and consider now the GPR model, $y = b(x)^T\beta + l(x)$, where $l(x) \sim \mathrm{GP}(0, k(x, x'))$ and $b(x) \in \mathbb{R}^p$. $k(x, x')$ is often parameterized by the hyperparameter, $\theta$, and thus might be written as $k(x, x'|\boldsymbol{\theta})$. In general, different algorithms estimate $\beta$, $\sigma^2$, and $\theta$ for model training and would allow specifications of $b$ and $k$ as well as initial values for parameters.

The current study explores four kernel functions, namely exponential, squared exponential, matern 5/2, and rational quadratic, whose specifications are listed in eqs 1−eqs 1, respectively, where $\sigma_l$ is the characteristic length scale defining how far apart $x$'s can be for $y$'s to become uncorrelated, $\sigma_f$ is the signal standard deviation, $r = \sqrt{(x_i - x_j)^T(x_i - x_j)}$, and $\alpha$ is a positive-valued scale-mixture parameter. Note that $\sigma_l$ and $\sigma_f$ should be positive. This could be enforced through $\theta$ such that $\theta_1 = \log \sigma_l$ and $\theta_2 = \log \sigma_f$.

$$k(x_i, x_j|\theta) = \sigma_f^2 \exp\left(-\frac{r}{\sigma_l}\right) \tag{1}$$

$$k(x_i, x_j|\theta) = \sigma_f^2 \exp\left[-\frac{1}{2}\frac{(x_i - x_j)^T(x_i - x_j)}{\sigma_l^2}\right] \tag{2}$$

$$k(x_i, x_j|\theta) = \sigma_f^2\left(1 + \frac{\sqrt{5}r}{\sigma_l} + \frac{5r^2}{3\sigma_l^2}\right)\exp\left(-\frac{\sqrt{5}r}{\sigma_l}\right) \tag{3}$$

$$k(x_i, x_j|\theta) = \sigma_f^2\left(1 + \frac{r^2}{2\alpha\sigma_l^2}\right)^{-\alpha} \tag{4}$$

Similarly, four basis functions are investigated here, namely, empty, constant, linear, and pure quadratic, whose specifications are listed in eqs 5−eqs 5, respectively, where $B = (b(x_1), b(x_2), ..., b(x_n))^T$, $X = (x_1, x_2, ..., x_n)^T$, and

$$X^2 = \begin{pmatrix} x_{11}^2 & x_{12}^2 & \cdots & x_{1d}^2 \\ x_{21}^2 & x_{22}^2 & \cdots & x_{2d}^2 \\ \vdots & \vdots & \vdots & \vdots \\ x_{n1}^2 & x_{n2}^2 & \cdots & x_{nd}^2 \end{pmatrix}$$

.

$$B = \text{empty matrix} \tag{5}$$

$$B = I_{n\times 1} \tag{6}$$

$$B = [1, X] \tag{7}$$

$$B = [1, X, X^2] \tag{8}$$

To estimate $\beta$, $\sigma^2$, and $\theta$, the marginal log-likelihood function in eq 9 is to be maximized, where $K(X,X|\theta)$ is the covariance function matrix given by $\begin{pmatrix} k(x_1, x_1) & k(x_1, x_2) & \cdots & k(x_1, x_n) \\ k(x_2, x_1) & k(x_2, x_2) & \cdots & k(x_2, x_n) \\ \vdots & \vdots & \vdots & \vdots \\ k(x_n, x_1) & k(x_n, x_2) & \cdots & k(x_n, x_n) \end{pmatrix}$.

The algorithm first computes $\hat{\beta}(\theta, \sigma^2)$, maximizing the log-likelihood function with respect to $\beta$ given $\theta$ and $\sigma^2$. It then obtains the $\beta$-profiled likelihood, $\log\{P(y|X, \hat{\beta}(\theta, \sigma^2), \theta, \sigma^2)\}$, which is to be maximized over $\theta$ and $\sigma^2$ to compute their estimates.

$$\log P(y|X, \beta, \theta, \sigma^2) = -\frac{1}{2}\{(y - B\beta)^T[K(X, X|\theta) + \sigma^2 I_n]^{-1}(y - B\beta)\} - \frac{n}{2}\log 2\pi - \frac{1}{2}\log|K(X, X|\theta) + \sigma^2 I_n| \tag{9}$$

### 5.2. Performance Evaluation.

Performance of the proposed GPR models is evaluated using the root-mean-square error (RMSE), mean absolute error (MAE), and correlation coefficient (CC) in eqs 10−eq 9, respectively, where $n$ is the number of data points, $a_i^{exp}$ and $a_i^{est}$ are the $i$th ($i = 1, 2, ..., n$) experimental and estimated energy band gap, and $\overline{a^{exp}}$ and $\overline{a^{est}}$ are their averages.

$$\mathrm{RMSE} = \sqrt{\frac{1}{n}\sum_{i=1}^{n}(a_i^{exp} - a_i^{est})^2} \tag{10}$$

$$\mathrm{MAE} = \frac{1}{n}\sum_{i=1}^{n}|a_i^{exp} - a_i^{est}| \tag{11}$$

$$\mathrm{CC} = \frac{\sum_{i=1}^{n}(a_i^{exp} - \overline{a^{exp}})(a_i^{est} - \overline{a^{est}})}{\sqrt{\sum_{i=1}^{n}(a_i^{exp} - \overline{a^{exp}})^2 \sum_{i=1}^{n}(a_i^{est} - \overline{a^{est}})^2}} \tag{12}$$

## AUTHOR INFORMATION


### Corresponding Authors

**Yun Zhang** − *North Carolina State University, Raleigh, North Carolina 27695, United States*; orcid.org/0000-0002-9464-1751; Email: yzhang43@ncsu.edu

**Xiaojie Xu** − *North Carolina State University, Raleigh, North Carolina 27695, United States*; Email: xxu6@ncsu.edu

Complete contact information is available at: https://pubs.acs.org/10.1021/acsomega.0c01438


### Notes

The authors declare no competing financial interest.

## ACKNOWLEDGMENTS

There is no funding received for this study.

## REFERENCES


(1) Devi, L. G.; Kavitha, R. Review on modified N-$TiO_2$ for green energy applications under UV/visible light: selected results and reaction mechanisms. *RSC Adv.* **2014**, *4*, 28265−28299.

(2) Bahnemann, D. Photocatalytic water treatment: solar energy applications. *Sol. Energy* **2004**, *77*, 445−459.

(3) Hay, S. O.; Obee, T.; Luo, Z.; Jiang, T.; Meng, Y.; He, J.; Murphy, S. C.; Suib, S. The viability of photocatalysis for air purification. *Molecules* **2015**, *20*, 1319−1356.
(4) Li, K.; Peng, B.; Peng, T. Recent advances in heterogeneous photocatalytic $CO_2$ conversion to solar fuels. *ACS Catal.* **2016**, *6*, 7485−7527.
(5) Roose, B.; Pathak, S.; Steiner, U. Doping of $TiO_2$ for sensitized solar cells. *Chem. Soc. Rev.* **2015**, *44*, 8326−8349.
(6) Parkin, I. P.; Palgrave, R. G. Self-cleaning coatings. *J. Mater. Chem.* **2005**, *15*, 1689−1695.
(7) Guo, W.; Kirste, R.; Bryan, Z.; Bryan, I.; Gerhold, M.; Collazo, R.; Sitar, Z. Nanostructure surface patterning of GaN thin films and application to AlGaN/AlN multiple quantum wells: A way towards light extraction efficiency enhancement of III-nitride based light emitting diodes. *J. Appl. Phys.* **2015**, *117*, No. 113107.
(8) Sheikhi, M.; Guo, W.; Dai, Y.; Cui, M.; Hoo, J.; Guo, S.; Xu, L.; Liu, J.; Ye, J. Mechanism of Improved Luminescence Intensity of Ultraviolet Light Emitting Diodes (UV-LEDs) Under Thermal and Chemical Treatments. *IEEE Photonics J.* **2019**, *11*, 1−8.
(9) Janczarek, M.; Kowalska, E. On the origin of enhanced photocatalytic activity of copper-modified titania in the oxidative reaction systems. *Catalysts* **2017**, *7*, No. 317.
(10) Lin, Y.-H.; Tseng, T.-K.; Chu, H. Photo-catalytic degradation of dimethyl disulfide on S and metal-ions co-doped $TiO_2$ under visible-light irradiation. *Appl. Catal., A* **2014**, *469*, 221−228.
(11) Hanaor, D. A.; Sorrell, C. C. Review of the anatase to rutile phase transformation. *J. Mater. Sci.* **2011**, *46*, 855−874.
(12) Ohtsuka, Y.; Fujiki, Y.; Suzuki, Y. Impurity effects on anatase-rutile transformation. *J. Jpn. Assoc. Mineral. Petrol. Econ. Geol.* **1982**, *77*, 117−124.
(13) Yu, L.; Yang, X.; He, J.; He, Y.; Wang, D. One-step hydrothermal method to prepare nitrogen and lanthanum co-doped $TiO_2$ nanocrystals with exposed {0 0 1} facets and study on their photocatalytic activities in visible light. *J. Alloys Compd.* **2015**, *637*, 308−314.
(14) Ilkhechi, N. N.; Alijani, M.; Kaleji, B. K. Optical and structural properties of $TiO_2$ nanopowders with Co/Ce doping at various temperature. *Opt. Quantum Electron.* **2016**, *48*, No. 148.
(15) Ilkhechi, N. N.; Kaleji, B. K.; Salahi, E.; Hosseinabadi, N. Comparison of optical and structural properties of Cu doped and Cu/Zr co-doped $TiO_2$ nanopowders calcined at various temperatures. *J. Sol-Gel Sci. Technol.* **2015**, *74*, 765−773.
(16) Oseghe, E. O.; Ndungu, P. G.; Jonnalagadda, S. B. Synthesis of mesoporous Mn/$TiO_2$ nanocomposites and investigating the photocatalytic properties in aqueous systems. *Environ. Sci. Pollut. Res.* **2015**, *22*, 211−222.
(17) Lei, X.; Xue, X.; Yang, H. Preparation and characterization of Ag-doped $TiO_2$ nanomaterials and their photocatalytic reduction of Cr (VI) under visible light. *Appl. Surf. Sci.* **2014**, *321*, 396−403.
(18) Hao, C.; Li, J.; Zhang, Z.; Ji, Y.; Zhan, H.; Xiao, F.; Wang, D.; Liu, B.; Su, F. Enhancement of photocatalytic properties of $TiO_2$ nanoparticles doped with $CeO_2$ and supported on $SiO_2$ for phenol degradation. *Appl. Surf. Sci.* **2015**, *331*, 17−26.
(19) Gu, D.-E.; Yang, B.-C.; Hu, Y.-D. V and N co-doped nanocrystal anatase $TiO_2$ photocatalysts with enhanced photocatalytic activity under visible light irradiation. *Catal. Commun.* **2008**, *9*, 1472−1476.
(20) Niu, Y.; Xing, M.; Tian, B.; Zhang, J. Improving the visible light photocatalytic activity of nano-sized titanium dioxide via the synergistic effects between sulfur doping and sulfation. *Appl. Catal., B* **2012**, *115*−*116*, 253−260.
(21) Tahir, M.; Amin, N. S. Photocatalytic $CO_2$ reduction with $H_2$ as reductant over copper and indium co-doped $TiO_2$ nanocatalysts in a monolith photoreactor. *Appl. Catal., A* **2015**, *493*, 90−102.
(22) Oseghe, E. O.; Ndungu, P. G.; Jonnalagadda, S. B. Photocatalytic degradation of 4-chloro-2-methylphenoxyacetic acid using W-doped $TiO_2$. *J. Photochem. Photobiol., A* **2015**, *312*, 96−106.
(23) Rangel-Vázquez, I.; Del Angel, G.; Bertin, V.; González, F.; Vázquez-Zavala, A.; Arrieta, A.; Padilla, J.; Barrera, A.; Ramos-Ramirez, E. Synthesis and characterization of Sn doped $TiO_2$ photocatalysts: Effect of Sn concentration on the textural properties and on the photocatalytic degradation of 2, 4-dichlorophenoxyacetic acid. *J. Alloys Compd.* **2015**, *643*, S144−S149.
(24) Kaleji, B. K.; Hosseinabadi, N.; Fujishima, A. Enhanced photocatalytic activity of $TiO_2$ nanostructured thin films under solar light by Sn and Nb co-doping. *J. Sol-Gel Sci. Technol.* **2013**, *65*, 195−203.
(25) Ismail, A. A.; Bahnemann, D. W. Mesoporous titania photocatalysts: preparation, characterization and reaction mechanisms. *J. Mater. Chem.* **2011**, *21*, 11686−11707.
(26) Schwartz, J.; Koch, C. C.; Zhang, Y.; Liu, X. Formation of Bismuth Strontium Calcium Copper Oxide Superconductors. U.S. Patent US9773962B2 (2017). https://patents.google.com/patent/US9773962B2/en (accessed May 19, 2020).
(27) Zhang, Y.; Johnson, S.; Naderi, G.; Chaubal, M.; Hunt, A.; Schwartz, J. High critical current density $Bi_2Sr_2CaCu_2O_x$/Ag wire containing oxide precursor synthesized from nano-oxides. *Supercond. Sci. Technol.* **2016**, *29*, No. 095012.
(28) Zhang, Y.; Koch, C. C.; Schwartz, J. Formation of $Bi_2Sr_2CaCu_2O_x$/Ag multifilamentary metallic precursor powder-in-tube wires. *Supercond. Sci. Technol.* **2016**, *29*, No. 125005.
(29) Zhang, Y.; Koch, C. C.; Schwartz, J. Synthesis of $Bi_2Sr_2CaCu_2O_x$ superconductors via direct oxidation of metallic precursors. *Supercond. Sci. Technol.* **2014**, *27*, No. 055016.
(30) Li, F.; Li, X.; Hou, M.; Cheah, K.; Choy, W. Enhanced photocatalytic activity of $Ce^{3+}$-$TiO_2$ for 2-mercaptobenzothiazole degradation in aqueous suspension for odour control. *Appl. Catal., A* **2005**, *285*, 181−189.
(31) Yu, J.; Jimmy, C. Y.; Leung, M. K.-P.; Ho, W.; Cheng, B.; Zhao, X.; Zhao, J. Effects of acidic and basic hydrolysis catalysts on the photocatalytic activity and microstructures of bimodal mesoporous titania. *J. Catal.* **2003**, *217*, 69−78.
(32) Ovenstone, J.; Yanagisawa, K. Effect of hydrothermal treatment of amorphous titania on the phase change from anatase to rutile during calcination. *Chem. Mater.* **1999**, *11*, 2770−2774.
(33) Yang, S.; Gao, L. Preparation of titanium dioxide nanocrystallite with high photocatalytic activities. *J. Am. Ceram. Soc.* **2005**, *88*, 968−970.
(34) Addamo, M.; Augugliaro, V.; Di Paola, A.; García-López, E.; Loddo, V.; Marci, G.; Molinari, R.; Palmisano, L.; Schiavello, M. Preparation, characterization, and photoactivity of polycrystalline nanostructured $TiO_2$ catalysts. *J. Phys. Chem. B* **2004**, *108*, 3303−3310.
(35) Munir, S.; Shah, S. M.; Hussain, H.; et al. Effect of carrier concentration on the optical band gap of $TiO_2$ nanoparticles. *Mater. Des.* **2016**, *92*, 64−72.
(36) Zhou, J.; Xie, L. Effect of net surface charge on particle sizing and material recognition by using phase Doppler anemometry. *Appl. Opt.* **2011**, *50*, 379−386.
(37) Tian, G.; Fu, H.; Jing, L.; Xin, B.; Pan, K. Preparation and characterization of stable biphase $TiO_2$ photocatalyst with high crystallinity, large surface area, and enhanced photoactivity. *J. Phys. Chem. C* **2008**, *112*, 3083−3089.
(38) Hu, S.; Li, F.; Fan, Z. Preparation of visible light responsive N doped $TiO_2$ via a reduction-nitridation procedure by nonthermal plasma treatment. *Appl. Surf. Sci.* **2011**, *258*, 1249−1255.
(39) Zhou, Z.; Li, M.; Guo, L. A first-principles theoretical simulation on the electronic structures and optical absorption properties for O vacancy and Ni impurity in $TiO_2$ photocatalysts. *J. Phys. Chem. Solids* **2010**, *71*, 1707−1712.
(40) Liu, L.-Y.; Zhang, Z.-X.; Gou, X.-F.; Yang, H.-X. Molecular modelling of the effect of loading rate on elastic properties of CNT-polyethylene nanocomposite and its interface. *Mater. Res. Express* **2020**, *6*, No. 1250d2.
(41) Ong, S. Materials Project. https://www.materialsproject.org/wiki/index.php/GGA%2BU_calculations#cite_note-1 (2016; accessed May 19, 2020).
(42) Wang, L.; Maxisch, T.; Ceder, G. Oxidation energies of transition metal oxides within the GGA+ U framework. *Phys. Rev. B* **2006**, *73*, No. 195107.


https://dx.doi.org/10.1021/acsomega.0c01438
*ACS Omega* 2020, 5, 15344−15352

(43) Zhang, Y.; Xu, X. Yttrium barium copper oxide superconducting transition temperature modeling through Gaussian process regression. *Comput. Mater. Sci.* **2020**, *179*, No. 109583.
(44) Zhang, Y.; Xu, X. Machine learning the magnetocaloric effect in manganites from lattice parameters. *Appl. Phys. A* **2020**, *126*, No. 341.
(45) Zhang, Y.; Xu, X. Predicting the thermal conductivity enhancement of nanofluids using computational intelligence. *Phys. Lett. A* **2020**, *384*, No. 126500.



https://dx.doi.org/10.1021/acsomega.0c01438
*ACS Omega* 2020, 5, 15344−15352